3D reconstruction of tropospheric cirrus clouds

M.N. Kouahla [a,*], M. Faivre [b], G. Moreels [c], H. Seridi [a]

[a] LabSTIC Laboratory, University of 08 May 1945 Guelma, Algeria
[b] Laboratoire Atmosphères, Milieux, Observations Spatiales, UPMC-CNRS, Paris, France
[c] University of Franche-Comté, Observatoire des Sciences de l'Univers THETA, Institut UTINAM – UMR CNRS 6213, Besançon Cedex, France

Abstract

In this paper, we present a series of results from stereo-imagery of cirrus clouds in the troposphere. These clouds are either of natural origin or are created by aircraft exhausts. They are presently considered to be a major cause for the climate change. Two observation campaigns were conducted in France in 2013 and 2014. The observing sites were located in Marnay (47°17′31.5″ N, 5°44′58.8″ E; altitude 275 m) and in Mont Poupet (46°58′31.5″ N, 5°52′22.7″ E; altitude 600 m). The distance between both sites was 36 km. We used numeric CMOS photographic cameras. The image processing sequence included a contrast enhancement and a perspective inversion to obtain a satellite-type view. Finally, the triangulation procedure was used in an area that is a common part of both fields of view.
© 2016 COSPAR. Published by Elsevier Ltd. All rights reserved.

Keywords: Cirrus; Stereovision System; 3D reconstruction

1. Introduction

Cirrus clouds are mainly composed of ice particles. They are located in the high troposphere and, sometimes, in the lower stratosphere, between 6 and 10 km high (Keckhut et al., 2005). They appear as bands, filaments or veils having a geographical extent as large as 50% (Stubenrauch et al., 2013). It is presently recognized that these clouds influence the climate (Ramanathan and Collins, 1991). They interact with aerosols in heterogeneous chemistry reactions. Small organic molecules such as methanol, formaldehyde or formic acid may be adsorbed at the surface of the ice grains. In addition, "artificial" cirrus clouds are created by the airplane trails, which results in an additional contribution to the heterogeneous phase photochemical processes (Sassen, 1997).

The cirrus clouds cover 20–30% of the Earth (Dowling and Radke, 1990; Wylie and Menzel, 1999). These clouds continue to be the focus of many efforts estimating the role of clouds in the earth's radiation budget.

In the recent years, ground-based instruments available for the measurement of clouds include radars, laser based instruments such as ceilometers (Liu et al., 2015) or LIDARs (Sunilkumar and Parameswaran, 2005). With these instruments, the algorithms applied to retrieve cloud parameters such as optical thickness and effective diameter of ice crystals, assume that clouds are homogeneous. For example, the CALIPSO satellite provides information on the impact of clouds and aerosols on Earth's climate, most of the conducted studies are based on the lidar methods (Cadet et al., 2005).

In this paper, we are interested in computing clouds altitude. The clouds composition depends on their altitude. High clouds like cirrus are always ice-crystal clouds (Cotton et al., 2011). Several observations are conducted in order to follow cloud evolution and define their

* Corresponding author. Tel.: +213 6 61 36 26 90; fax: +213 37 20 11 68.
E-mail addresses: Kouahla.mohammednadjib@univ-guelma.dz, Kouahla.nadjib@yahoo.fr (M.N. Kouahla).

characteristics. With this aim, recent analyses of satellite data (AIM satellite) and many lidar techniques have been developed to retrieve cirrus parameters such as the ice water content (IWC) and ice crystal sizes and shapes.

The altitude of a cloud is a key parameter in the characterization of clouds (Hirsch et al., 2011). It is an indicator of cloud type and is useful to classify cloud processes (Tapakis and Charalambides, 2013).

In addition, the altitude of clouds has crucial importance for the computation of cloud motion winds (Menzel, 2001) and for precipitation estimation (Manoj et al., 2010), for climate studies (Fontana et al., 2013) and aviation safety (Schafer et al., 2004).

These clouds affect climate in the troposphere, the temperature decreases with altitude. With the same optical properties cirrus clouds emit at lower temperature at high altitude than at low altitude (Fauchez et al., 2014).

We completed these studies by stereoscopic imaging method to determine the altitude of natural cirrus clouds or artificial along an aircraft trajectory and to obtain a 3D representation of the surface.

2. Measuring cirrus and aircraft trails with a stereoscopic set of cameras

In the present paper, we present the first phase of a program that aims at analyzing the local influence of aircraft exhausts on the upper tropospheric and/or lower stratospheric medium.

The physico-chemical composition of the medium will simultaneously be measured by a lidar.

In the following, we describe a stereo-imaging method for measuring the altitude of cirrus created by aircraft exhausts and of natural cirrus present in the same area. As the position of the aircraft is, a priori, not precisely defined, we use CCD photographic cameras providing 35.13°*23.84° fields of view. The stereo-imaging method and subsequent numeric treatment are described in detail. An aircraft trail is observed from two ground-based sites located in the Jura region, in Marnay and Mont Poupet. Its geometric parameters are determined using a triangulation algorithm. In a further phase of the project, the same type of measurements will be conducted from two sites: Simiane and Canta Galet close to the LATMOS atmospheric laboratory in Saint Michel l'Observatoire, where a vertical lidar is currently under operation. Using two photographic cameras in a vis-à-vis mode permits to have a field-of-view wide enough to encompass both the lidar ray and an eventual aircraft trail which, generally, will not be secant lines (Fig. 6).

The problem of retrieving 3D information of an object or a scene using a set of 2D images is an important research theme in computer vision. Several methods have been developed to provide a stereoscopic reconstruction of a 3D object. These methods generally use two images of the object of interest simultaneously taken with two cameras or two views of the object in motion taken with a single camera (Park and Kweon, 2001; Fanany and Kumazawa, 2004).

Pairs of points of the object need to be located in both images. The 3D restitution of the shape of the object is obtained in using the properties of projective geometry. The process is made easier when the object presents specific features such as lines, edges, corners or apexes for which the identification of matched points in the images may be evident (Faugeras et al., 1993).

Stereo vision systems have demonstrated their ability in a large number of applications in medical imaging (Ghanem et al., 2003), objects reconstruction (Fua and Leclerc, 1995), obstacle detection (Perrollaz et al., 2006), and mobile robots (Mallet et al., 2000).

In this paper, we present an application of a stereoscopic vision system that was developed to reconstruct a 3D model of an object which is typically a tropospheric cloud extended in a limited altitude range as a result of the stratification of the troposphere. Unlike a solid object, a cirrus cloud is a diffuse medium with no precisely defined contour.

The first application of this type of system was on OH emissive layer observed in Peru in 2005–2006 whose altitude is comprised between 82 and 92 km. Two CCD cameras were installed in the vis-à-vis mode in two sites distant from 645 km in Peru: Cerro Cosmos around Huancayo and Cerro Verde Tellolo around Arequipa, the average altitude of the layer was determined and relief maps were obtained to study the dynamic aspect of the emissive layer, the intensity variation and movement of waves were observed during the night (Moreels et al., 2008; Kouahla et al., 2010).

Our aim is to develop and use a ground-based stereo imaging tool suitable to study dynamic processes occurring in the atmosphere such as winds, density waves, tides, turbulence.

The paper is organized as follows: Section 2 is devoted to the brief description of the stereoscopy vision system consisting of two cameras oriented in face to face mode in which the principles of the inversion of perspective, epipolar geometry, and measure of correlation are explained in detail. Section 3 describes the instrumentation and observation sites. In Section 4, the research focuses on the upper troposphere where cirrus clouds are frequently observed. In June 2014, two observation campaigns were conducted in France; the distance between the observation sites is equal to 35.52 km. It is shown on an example that the altitude of a cirrus layer may be determined with a precision of ±300 m in calculating the similarity measure. Some results are presented, and a comparison is made between the correlation coefficients. Finally, in Section 5, we present some concluding remarks about the proposed method.

3. Stereoscopy vision system for observing an tropospheric layer

Our aim is to retrieve a relief surface map of a tropospheric layer using images of the sky taken at two distant

geographical sites. Many developed approaches have used the digital cameras as an instrument of measure. For instance, Ehrlich et al. (2012) installed a camera on an airplane to construct a bi-directional reflectance distribution function for cloud. Kataoka et al. (2013) developed a method for estimating the altitude of visible aurorae from data obtained by a pair of DSLR cameras.

Like all photographs, these images do not directly provide information related to the altitude, thickness, ice crystal size, vertical extent and density of the medium that the layer is made of. Our purpose will be to use pairs of images of the same area to retrieve a "surface relief" map, comparable to the geographic maps showing plaster-molded mountain range, hills and canyons. The thickness of the tropospheric layer under consideration is small compared to its mean altitude, i.e. $\sim$1 to 2 km for a cirrus layer located between 6 and 10 km (Keckhut et al., 2005).

Starting with the image obtained simultaneously at two sites looking at the same region in the sky, we use four tools to retrieve the relief of the layer both types of cameras, real and virtual.

(a) We use the perspective projection geometry with real cameras;
(b) We introduce the concept of "virtual camera" that represents a cametra located at an altitude L above the ground level to restitute the real appearance of the layer and uses an inversion of the perspective projection (Pautet and Moreels, 2002);
(c) We use epipolar geometry;
(d) We calculate a disparity parameter, i.e. a zero normalized correlation coefficient (ZNCC) to retrieve the altitude of the layer barycenter.

3.1. Image capture of the tropospheric layer

Let us first introduce the tri-dimensional frame that is generally called "world frame". Its origin is the center of the earth. The coordinates of a point in this frame will be referred to using capital letters i.e. (X, Y, Z). Secondly, let us define a frame (x_r, y_r, z_r) associated with the camera used to capture the images; called "real camera frame". The coordinates of points in this frame are noted in lower case letters. The camera lens makes a projection of the object of interest, i.e. a quadrangle area of the specific emissive layer on the sensitive CCD surface of the camera. A pinhole model shows that the light rays are represented by straight lines. For the sake of figure clarity, the image plane is represented, non-inverted, on the same side as the object with respect to the pinhole (Tsai, 1987; Beyer, 1992).

Thirdly, we define a frame (u, v) associated with the CCD retina image plane. The coordinates of a point in this frame are given as pixel numbers and are counted from the upper left corner. The center of the image frame is the intercept of the image plane with the optical axis of the camera. Its coordinates are u_0 and v_0 (Fig. 1).

3.2. Inversion of the perspective

In order to describe the real camera which is used to take the series of images of the observed cloud, we introduce a pinhole model. The perspective projection equations giving the coordinates (u, v) in the retinal plane of an observed point having as coordinates $x_r' = (x'_r, y'_r, z'_r)^t$ are as follows.

Let us first define the emissive matrix of the real camera:

$$K = \begin{pmatrix} k_u & 0 & 0 & u_0 \\ 0 & k_v & 0 & v_0 \\ 0 & 0 & 0 & 1 \end{pmatrix} \quad \text{where } k_u, \ k_v,$$

k_u is the horizontal scale factor, k_v is the vertical scale factor (here $k_u = k_v = 52.63$ pixels/mm); f is the focal length of the employed lens, u_0, v_0 are the horizontal and vertical numbers of the central pixel.

The figures k_u, k_v and f are called intrinsic parameters of the camera.

The expressions for the horizontal/vertical pixel coordinates u and v are the following:

$$u = k_u f \frac{x_r}{z} + u_0, \quad v = k_v f \frac{y_r}{z} + v_0$$

Let us introduce homogenous coordinates S_u, S_v and S where $S = 1/f$ is the scale parameter. We obtain a matrix relation between the coordinates of the observed point (x_r, y_r, z_r) in the camera frame and its position (u, v) in the image (Ma, 2004):

$$\begin{pmatrix} S_u \\ S_v \\ S \end{pmatrix} = \begin{pmatrix} K_u f & 0 & u_0 & 0 \\ 0 & K_v f & v_0 & 0 \\ 0 & 0 & 1 & 0 \end{pmatrix} \begin{pmatrix} x_r \\ y_r \\ z_r \\ 1 \end{pmatrix}$$

We now introduce the concept of "virtual camera" vertically located above the real camera at an altitude L above the earth ground level. The optical axis of the virtual camera contains the optical center of the real camera (Fig. 1). The whole scheme may be compared to a cosmonaut inside a space vehicle taking pictures of the earth downwards in the nadir direction (Pautet and Moreels, 2002).

Here, we assume that the characteristics of both cameras are coherent with the size of the CCD retina. We chose the altitude L of the virtual camera so that the fields of view of the real ground based camera and of the virtual space borne cameras coincide. Let us call $(x_{max}, y_{max}, z_{max})$ the coordinates of the farthest away point present in the "real" image. The altitude L of the virtual camera associated with a real camera is calculated in using the following equations
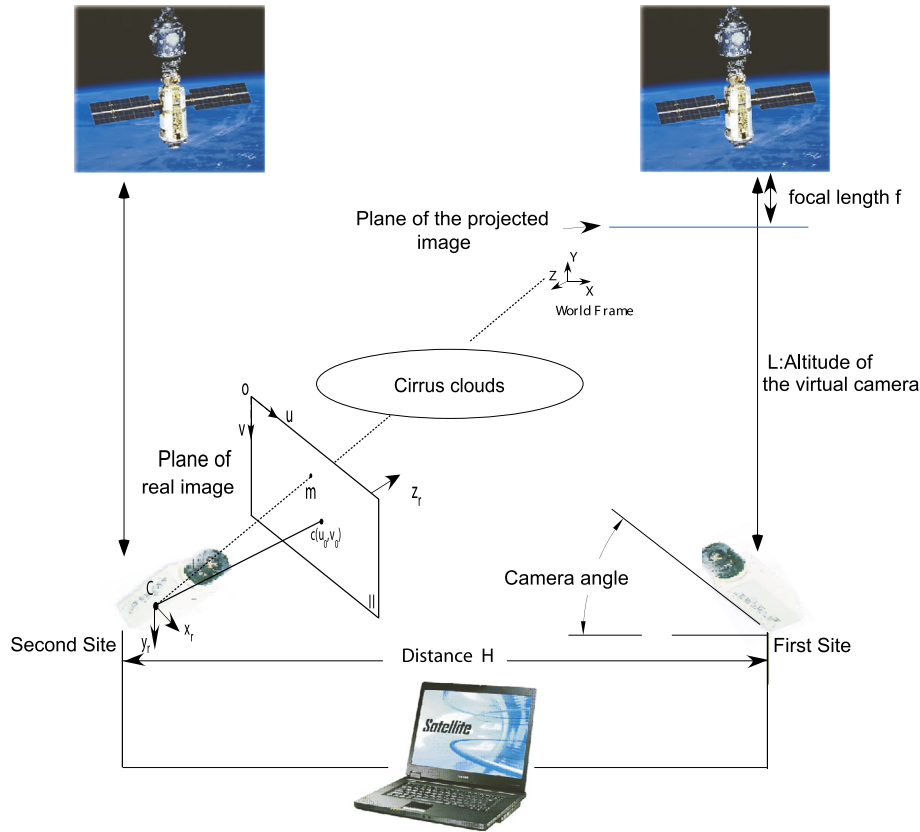
Fig. 1. Schema of proposed Stereovision System.

$$L = \left(f - y_{\max} + f \frac{z_{\max}}{Y_{\max}} \right)$$

$$y_{\max} = \frac{R_h^2 - R_T^2}{R_h} \left(1 + \sqrt{\frac{R_h^2 - R_T^2}{R_H^2 - R_T^2}} \right)$$

$$z_{\max} = \frac{R_T}{R_h} \sqrt{R_h^2 - R_T^2} \left(1 + \sqrt{\frac{R_h^2 - R_T^2}{R_H^2 - R_T^2}} \right)$$

$$Y_{\max} = \text{size of pixel} * (\text{Number of pixels}/2)$$

Where H: height of observed layer, h: altitude of observation site, R_T: radius of the earth, $R_h = R_T + h$, $R_H = R_T + H$.

In the case of the tropospheric cirrus whose altitude is comprised between 6 and 10 km, altitude of observation site: 275 m, size of pixels: 5.7 μm, Focal length = 35 mm, image size = 4096*4096 pixels, we find a value $L = 250$ km for the virtual camera. This leads to an adequate matching of the image pairs used in the stereoscopic restitution process.

Let us introduce a set of two cameras that are, in our case, two virtual cameras located well above the tropospheric layer under consideration. The retinal image planes of the cameras are called π_1 (right hand) and π_2 (left hand). The system is ruled by epipolar geometry under perspective projection. Let us consider a point M of the layer. Its image given by the right-hand camera is a point called m_1 (Fig. 2).

Through the epipolar geometry, the point m_1 determines, in the left-hand view, a line $m_2 E_2$ called epipolar line related to the point m_1.
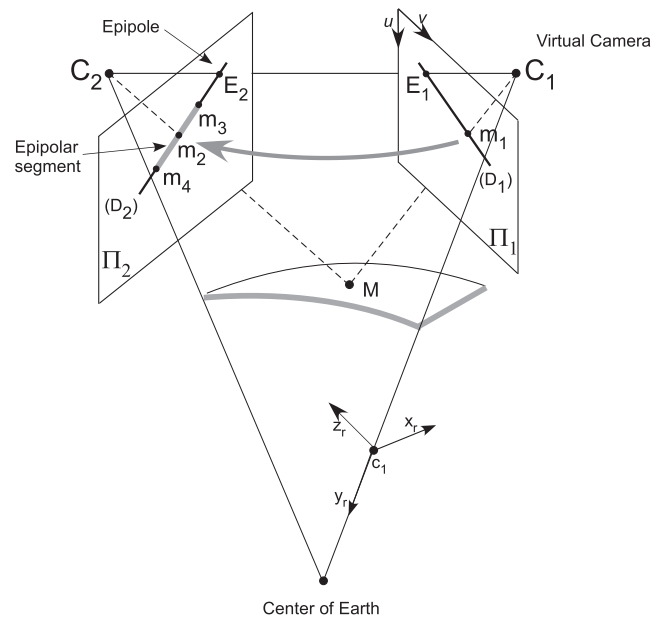

Fig. 2. Principle of epipolar geometry.

The line joining the optical centers C_1 and C_1 of both cameras is called the baseline. The plane which contains the baseline and the point M, m_1 and m_2 is called an "epipolar plane" (Hartley and Zisserman, 2003). The intersection of the baseline $C_1 C_2$ with the image plane π_2 is called the epipole related to the line $C_1 m_1$ M.

The epipolar constraint states that, for a point m_1 in the first image, its correspondence point m_2 in the second image is located on the epipolar segment. As a result, the search space for a correspondence is reduced from 2 dimensions to 1 dimension.

An additional constraint is imposed by the chemical and physical properties of the tropospheric layers under consideration. The cirrus clouds, for instance, are located in the altitude range 6–10 km, as shown by satellite observations. This limits the possible position of the point matched with m_1 to the epipolar segment m_3m_4 in the left-hand image π_2.

3.3. Epipolar geometry and 3D reconstruction

The epipolar geometry is defined by the optical centers C_1 and C_2 and by the perspective projection matrix P which is invertible. The first step consists in calculating the equation of the optical line (CM) that joins the optical center C and the current pixel m in the image (Faugeras, 1994). The equation is:

$$(Cm) = \{W = C + \lambda P^{-1}\tilde{m};\ \lambda \in [\lambda_{\min}, \lambda_{\max}]\}$$

The second step consists in finding the position of the matching point of m in the second image. It requires the calculation of a disparity parameter which is a correlation exertion. In the present case, the object is diffuse and does not contain any definite easily recognizable features such as points, lines, and apexes. We use a disparity parameter called ZNCC, zero normalized cross-coefficient which is the product of the root-mean square of photonic intensities measured on small windows around matched points n both image (Ma, 2004). A comparison of correlation coefficients is detailed in Section 3.

Given a pixel m_1 in the right image π_1, the position of the matched point m_2 in the left image π_2 is sought along the epipolar segment m_3m_4 in calculating the ZNCC coefficient on square windows of dimensions $(2p + 1, 2p + 1)$ defined around the points m_1 and m_2 (Fig. 3). Matched pairs of points are identified by iteration when the ZNCC parameter is maximum.

Retrieving the altitude of the point M is explained in Fig. 3 which shows the two real ground-based cameras and the two corresponding virtual satellite cameras. Let m_1 be a pixel in the retinal plane of the right virtual camera m_1 is the image of geographic point M whose altitude is z. the matched point of m_1, called m_2, is localized in the retinal plane of the left camera on the epipolar segment in computing the ZNCC parameter. The altitude z_m is calculated knowing the position of the matched points m_1 and m_2.

4. Instrumentation and observation sites

Two photographic digital cameras (Canon 400D) are set-up in two sites distant 35.52 km. They are oriented in a face to face configuration so that the azimuths of their lines of sight differ by 180°. Their retina contains 3888*2592 square CMOS pixels of size 5.71*5.71 microm-
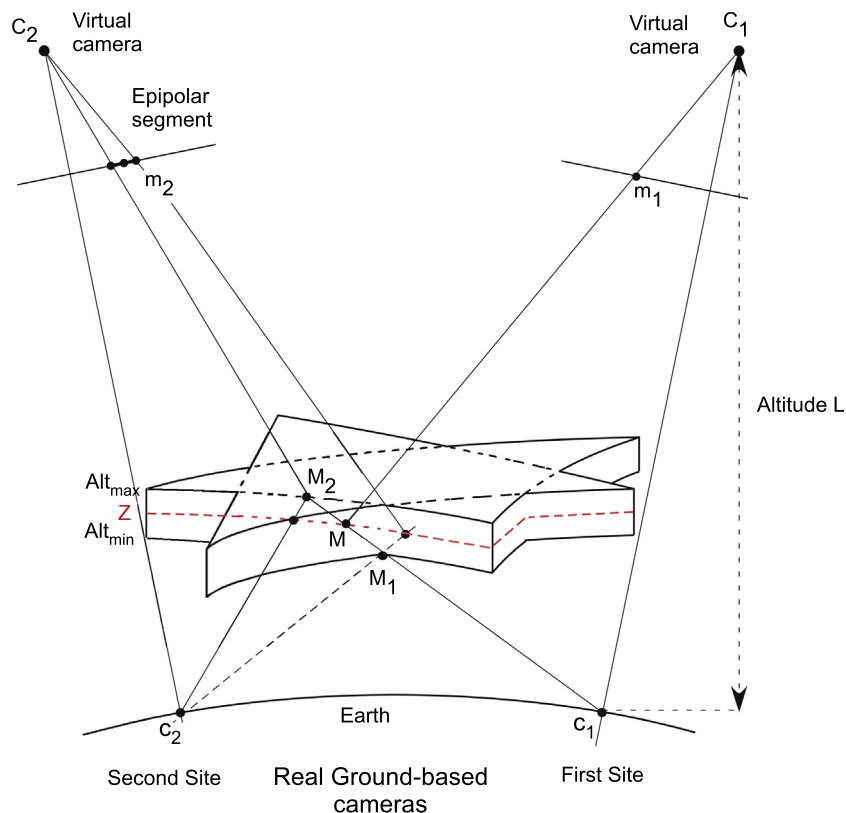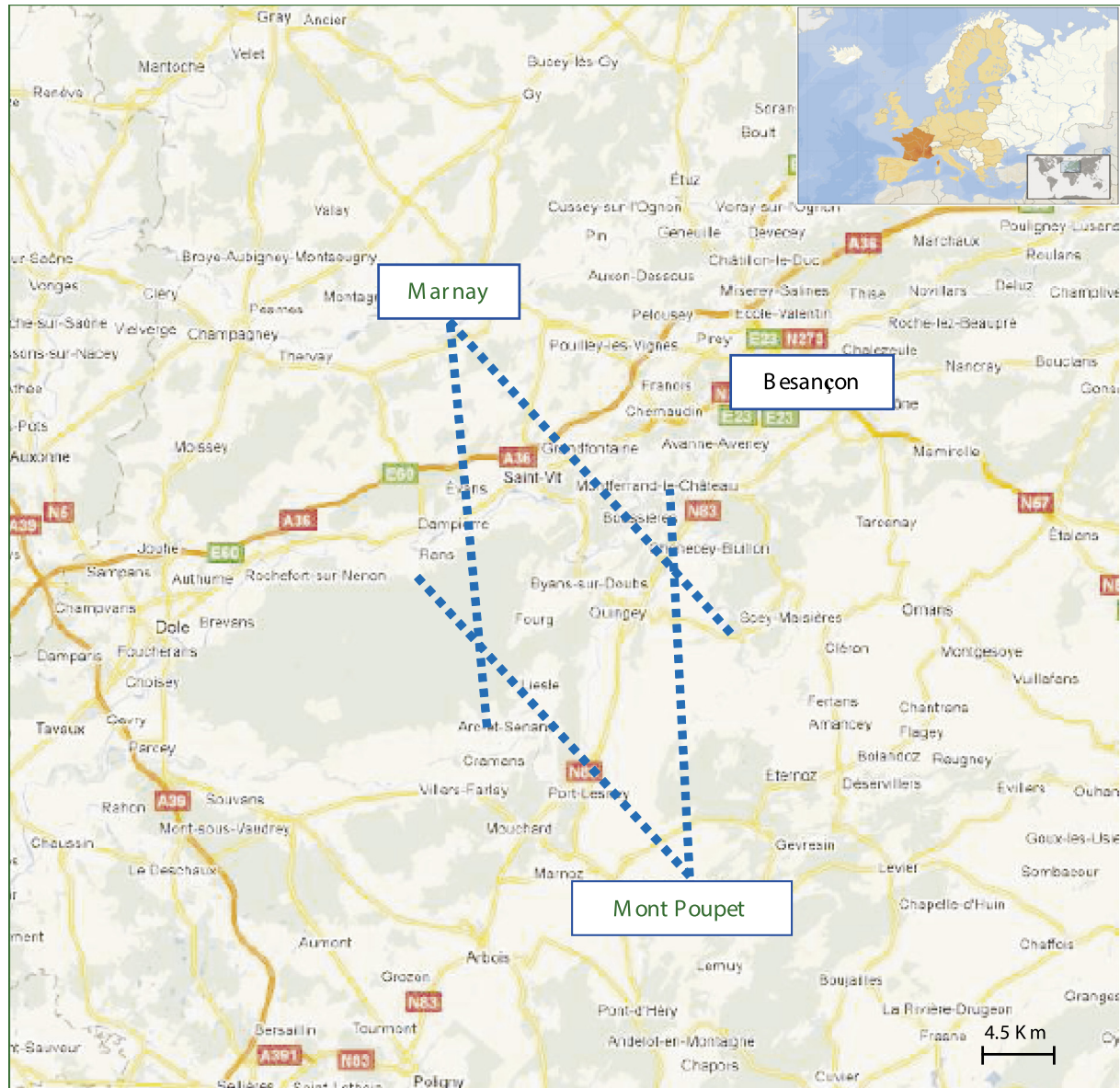

Fig. 3. System geometry.

Fig. 4. The observation sites: Marnay and Mont-Poupet.

eters. The camera is equipped with a lens having a 35 mm fixed focal length.

The field of view is 35.13° horizontally and 23.84° vertically. The lines of sight of both cameras are set at an elevation angle of 28°. The observation campaign was conducted in France in 2014. The first selected observation site is located in Marnay (47°17′47,7″ N, 5°44′58,8″ E) 25 km northwest of Besancon at an altitude of 275 m, and the second at Mont Poupet (46°58′31,5″ N, 5°52′22,7″ E) southwest of Besancon at 43 km and at an altitude of 600 m (Fig. 4).

5. First results of stereoscopic observations of tropospheric cirrus

Our observed objects are cirrus clouds produced at an altitude between 6 and 10 km in the troposphere. The origin of these clouds, constituted of ice particles is either natural, or connected with airplane exhausts.

We aim at establishing a relief map to obtain information on the structure of these clouds: diffuse structure, or in bands. We have developed a method to determine the average altitude of the centroid of the layer on a geographical area which corresponds, for example, to a square of 100*100 pixels.

5.1. Artificial cirrus clouds "aircraft trails"

Preliminary results related to a cirrus created by an airplane exhaust trail on June 11, 2014 at 19h49 (UT) are presented here after in Fig. 5. The simultaneous photographs taken in Marnay and Mont Poupet are shown in boxes (a) and (b). The geometric perspective is inverted in boxes
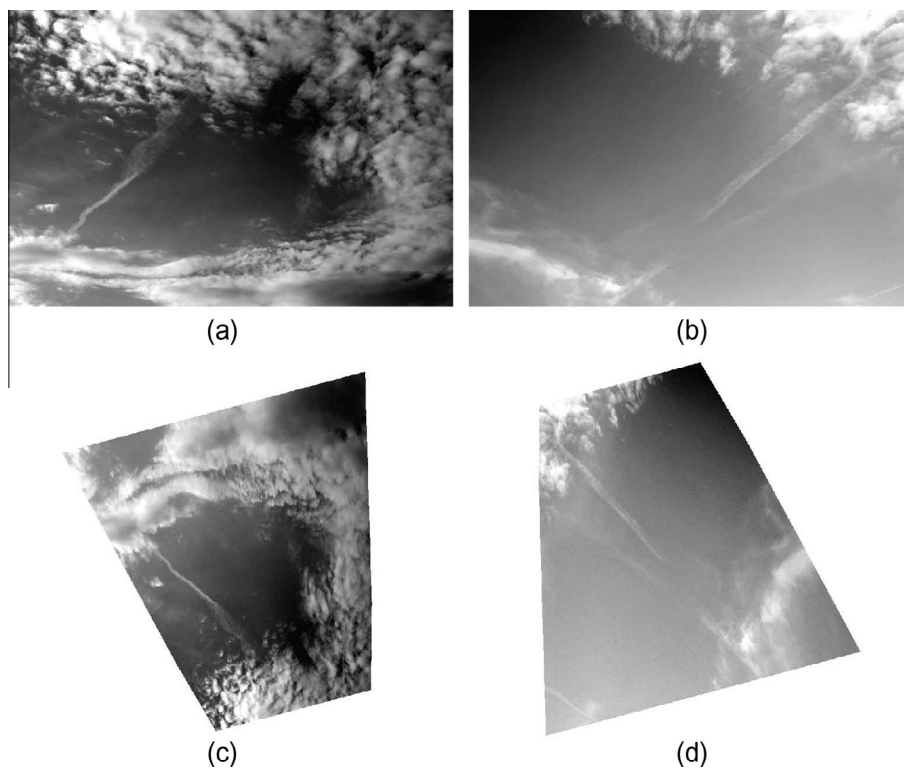
Fig. 5. Pair of cirrus image in 11 June 2014, 19h49 at Mont Poupet (a) and Marnay (b). The images in (c) and (d) correspond the satellite type views of (a) and (b).
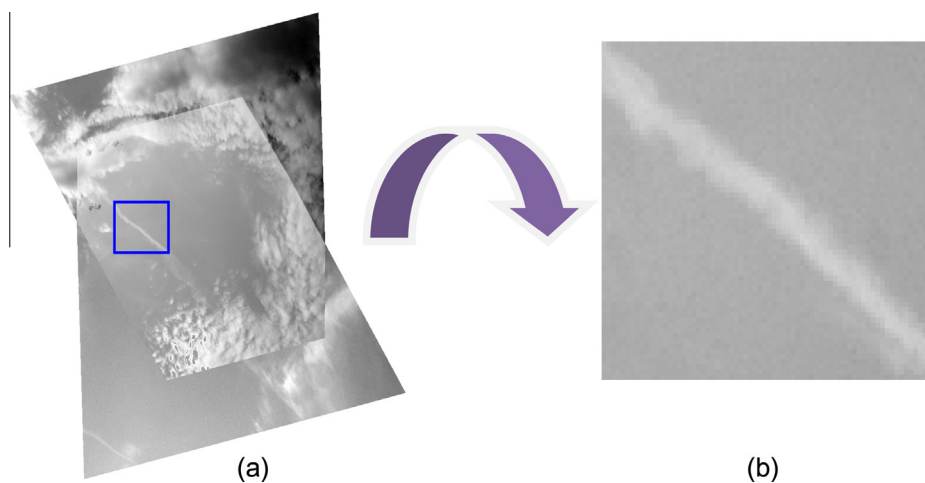

Fig. 6. (a) Superposition of the projected images (5.c) and (5.d). (b) Position of the square area inside the common zone of the projected images of Fig. 6a.

(c) and (d) which show the cirrus as would be seen from above by a cosmonaut in a spacecraft looking downward.

In Fig. 6, the views of (Fig. 5c and d) are superposed. The aircraft trail is apparent in the central left sector of the image. A 100*100 pixels area or 2.8*2.8 km² is defined in Fig. 6(a) and shown enlarged, in (b).

In Fig. 7, we present the results of the triangulation algorithm on the aircraft trajectory presented in Fig. 6. Panels 7.a (Mont Poupet) and 7.b (Marnay) exhibit pseudo-relief representations of the coded intensity shown in Fig. 5(c and d). The third panel, (7.c) shows the altitude of the ruffled surface of the aircraft trail, comprised between 8 and 10 km. The fourth panel, 7(d) is a cut of

the wave field perpendicularly to the crests. The mean altitude is 9.6 km.

There is an excellent agreement between the 3D surface map in panel (7.c) and the coded intensity diagrams in (7.a) and (7.b) the wave field is clearly apparent in the photometric images and in the 3D representation of the aircraft trail. These maps correspond to regions of 100 pixels a side; the size of the regions has been chosen to cover at least one trail and the elementary area on which we compute a cross correlation parameter (typically 5*5 pixels) is small in size relatively to the trail width. To avoid edge effects, the maps have been performed in the area where the calculation of the parameter ZNCC is not trimmed at the edges. Indeed,
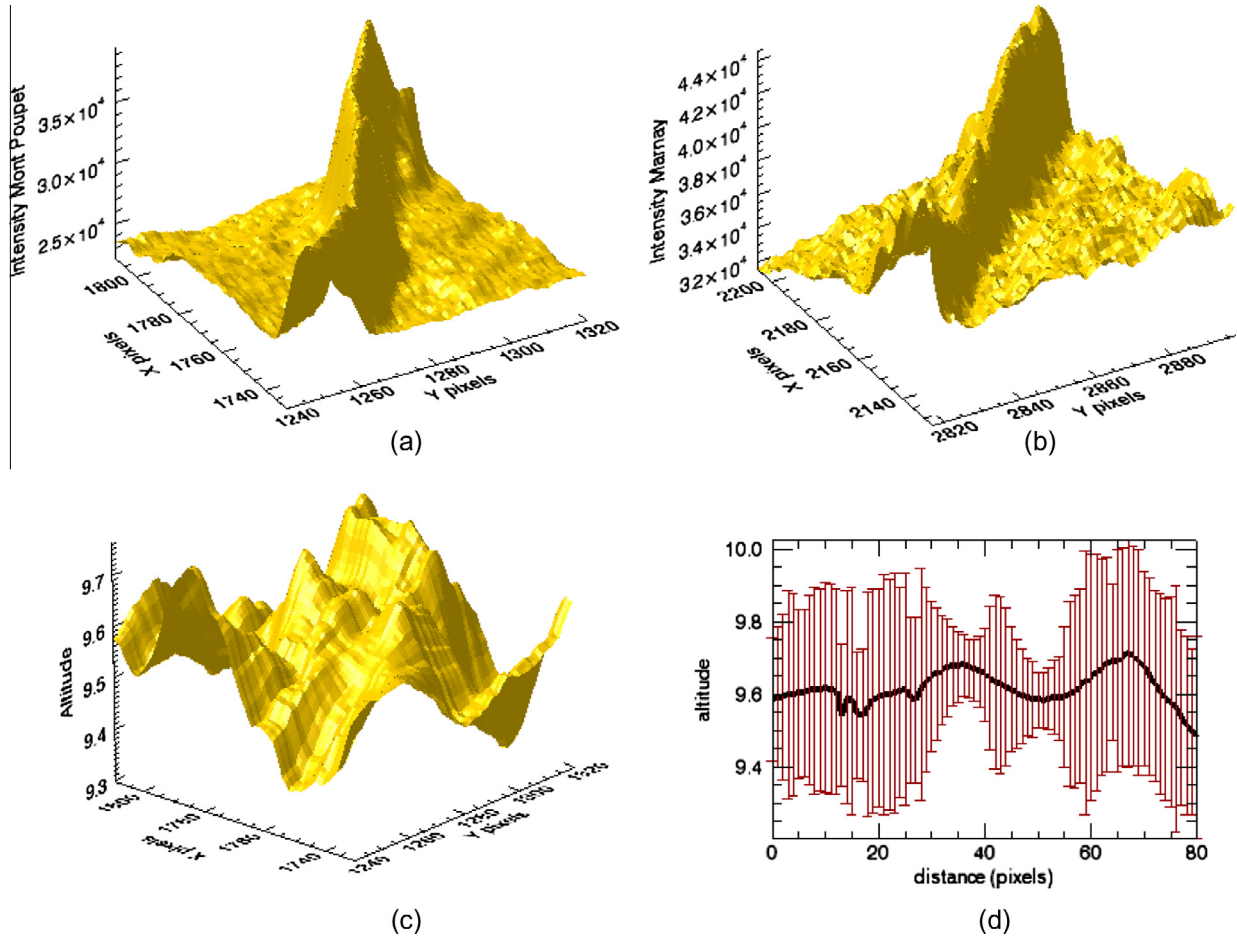
Fig. 7. 3D reconstruction of artificial cirrus: aircraft trajectory in 11 June 2014. Coded intensity diagrams of the simultaneous images recorded at Mont Poupet (a) and Marnay (b). In panel (c), a 3D reconstitution of the aircraft trajectory is presented. In panel (d), a cut of the relief map 7c.

the map of an area of 100 pixels is reduced to a square of 80*80 pixels.

5.2. Natural cirrus clouds

We present now a second set of results of the stereo-imaging application related to natural cirrus clouds.

In the same pair presented previously in Fig. 5, we choose a second area of the same size 100*100 pixels where cirrus clouds are apparent. In this area, we use the stereo imaging algorithm as explained in Section 2, but with parameters adjusted for the altitude range of the observed object.

Once this average altitude is determined, the triangulation algorithm enables establishing the relief map of the selected area. Since the cirrus object is diffuse, and does

not present any geometric mark such as a line, a plane or a wedge, we calculate the cross-correlation coefficient (ZNCC) to identify pairs of matched points in two images taken at the same instant in both sites.

The ZNCC is a quantitative criterion well-defined for comparing the different results obtained during the identification phase of pairs of points. The maximum possible value of ZNCC is 1, indicating coherence between the observed structures in the two projected images.

The applied ZNCC operator on two images is a product of zero normalized cross-correlation. The correlation measure is normalized by the product of the standard deviations of the measured intensities on the windows. The product of cross correlation measures the similarity between two signals.

$$\mathrm{ZNCC}(x,y,dx,dy) = \frac{\sum_{k=-p}^{p}\sum_{l=-p}^{p}(I_1(x+k,y+l)-\overline{I}_1)(I_2(x+d_x+k,y+d_y+l)-\overline{I}_2)}{\sqrt{\sum_{k=-p}^{p}\sum_{l=-p}^{p}(I_1(x+k,y+l)-\overline{I}_1)^2}\sqrt{\sum_{k=-p}^{p}\sum_{l=-p}^{p}(I_2(x+d_x+k,y+d_y+l)-\overline{I}_2)^2}}$$
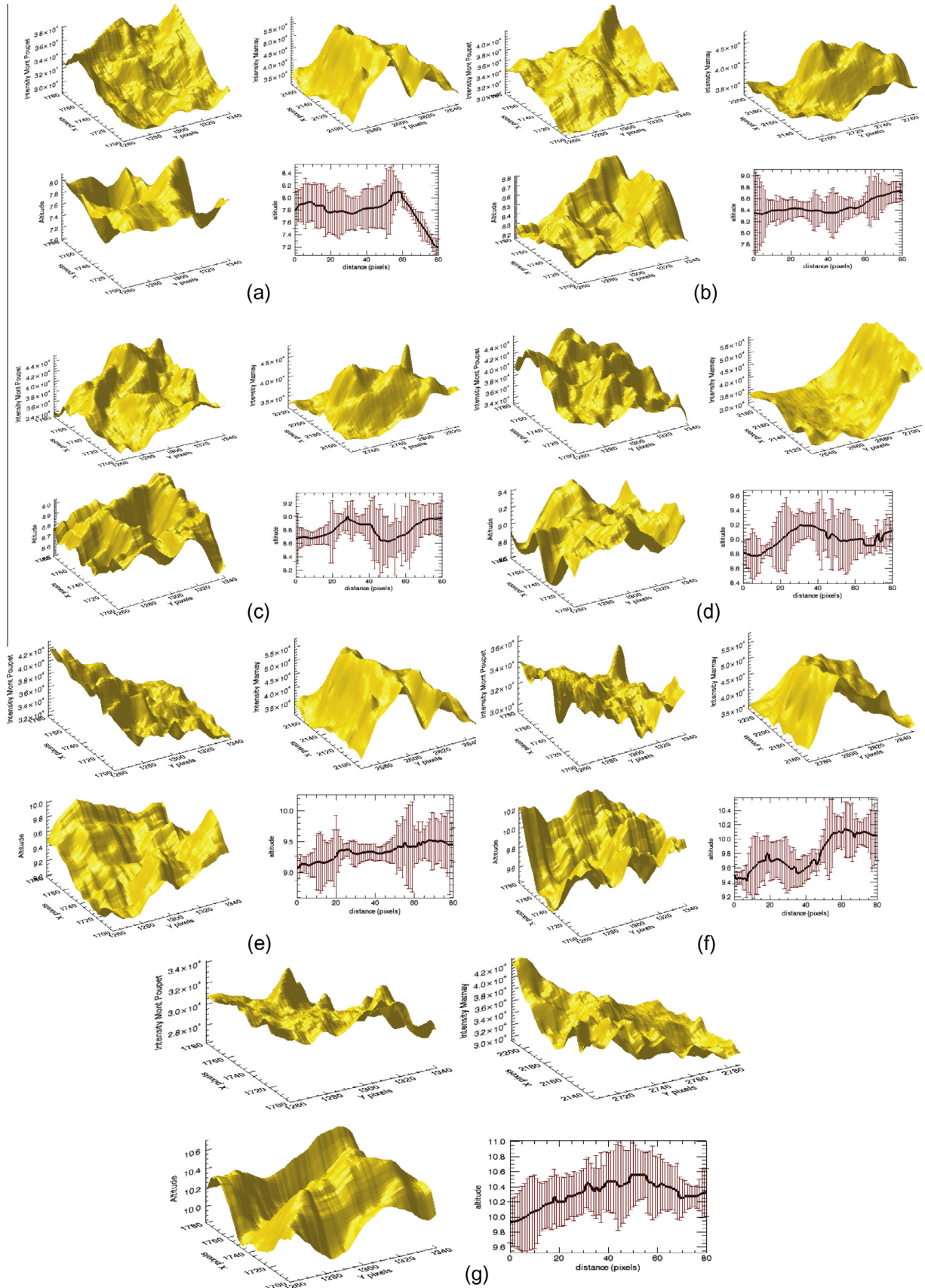
Fig. 8. Series of results by varying the average altitude: (a) $Alt_{moy} = 7.5 \pm 1$ km, (b) $Alt_{moy} = 8 \pm 1$ km, (c) $Alt_{moy} = 8.5 \pm 1$ km, (d) $Alt_{moy} = 9 \pm 1$ km, (e) $Alt_{moy} = 9.5 \pm 1$ km, (f) $Alt_{moy} = 10 \pm 1$ km, (g) $Alt_{moy} = 10.5 \pm 1$ km.

To determine the average altitude of cirrus clouds (altitude of the barycenter), we perform a series of tests on the observations of June 11, 2014. We calculate the ZNCC for a series of values of average altitude between 7.5 and 10.5 km at intervals of 500 m.

The results are presented in Fig. 8(a–g). Each figure compares the intensity map in pseudo relief, and the relief map of altitude obtained by stereo-imaging. The comparison between the results is presented in Fig. 9, which shows that the value of ZNCC is comprised between 0.57 and 0.67 and its maximum value corresponding to an altitude of the gravity center is 8.5 ± 1 km.

In Fig. 10, we note the coherence between the intensity representation and the relief of altitude and to be more consistent we added the ZNCC curve for the variation between the two intensities.

two basic measures: the Euclidean distance between the two vectors formed by the pixel intensities (ZSSD denoted as Zero Sum of Squared Differences), and the scalar product of two vectors (denoted by ZNCC, as zero normalized cross-correlation). Works related to the choice of correlation criteria have shown that the two correlation criteria mentioned above present best results (Aschwanden and Guggenbuhl, 1992). The tests realized on the two images, also show that the two correlation criteria ZNCC and ZSSD give the best results in average altitude, except that ZSSD remains effective under certain constraints of observation.

The ZSSD uses the local luminance to measure the similarity between two areas. The similarity measure associated with the sum of squared differences is applied to images satisfying an additional photometric criterion.

$$\text{ZSSD}(x, y, dx, dy) = \frac{\sum_{k=-p}^{p}\sum_{l=-p}^{p}\left(I_1(x+k, y+l) - I_2(u+d_x+k, y+d_y+l)\right)^2}{\sqrt{\sum_{k=-p}^{p}\sum_{l=-p}^{p}(I_1(x+k, y+l) - \overline{I_1})^2}\sqrt{\sum_{k=-p}^{p}\sum_{l=-p}^{p}(I_2(x+d_x+k, y+d_y+l) - \overline{I_2})^2}}$$

In the panels (10.a) and (10.c) the intensities at each site are shown in pseudo relief. A diagonal cut of these intensities is presented in panels (10.b) and (10.d).

The panel (10.e) presents the altitude of the centroid of the cloud on the same region of Fig. 10a and c. The panel (g) gives the value of the coefficient of cross-correlation (ZNCC) according to the diagonal cut used in the figures (b), (d) and (f).

5.3. Comparison between ZNCC and ZSSD

The similarity measure between two regions from two stereoscopic images is evaluated according to the choice of a correlation criterion which provides a good match in any situation. Most correlation criteria are derived from

P is the size of the correlation window. The higher the value of p, then the higher is the sensitivity of the operator to variation in intensity. The intensity functions of left and right images are respectively noted I_1 and I_r. The disparity value (d_x, d_y) is associated to the pixel m (x, y).

M_1 is the pixel (x, y) in the coordinate reference frame and m_2 $(x + dx, y + dy)$ in the associated pixel on the reference image plane. The vector (dx, dy) associated to the pixel m is called disparity. The disparity field associated to the point m is constrained by the epipolar geometry. For any pixel in the plane of the reference image, the entire disparity is a segment in the second image plane.

We propose to make a comparison between the two coefficients ZNCC and ZSSD using the same pair of images. We conduct three different tests and compare the obtained profiles with each coefficient.

- First test: Without change on images. The amplitude obtained with the SSD is 4.7 km, significantly larger than that obtained with the NCC.
- Second test: Adding a continuous component (offset) images. The average altitude of the layer changes from 8.66 km (without offset) to 8.54 km (with offset). The variation is much lower if one uses the coefficient SSD. The average altitude then goes from 8.59 km (without offset) to 8.62 km (with offset).
- Third test: Increasing the contrast of two images. It is observed that the results undergo significant change if one uses the SSD (Fig. 11).

The results of these tests are given in Table 1. One notices that using the coefficient NCC provides much more consistent results than the coefficient SSD. The
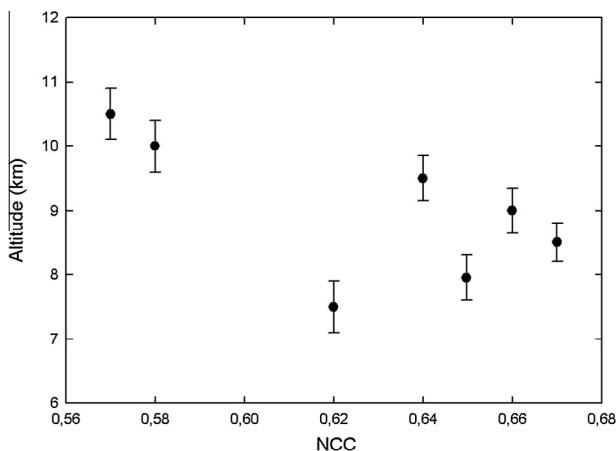

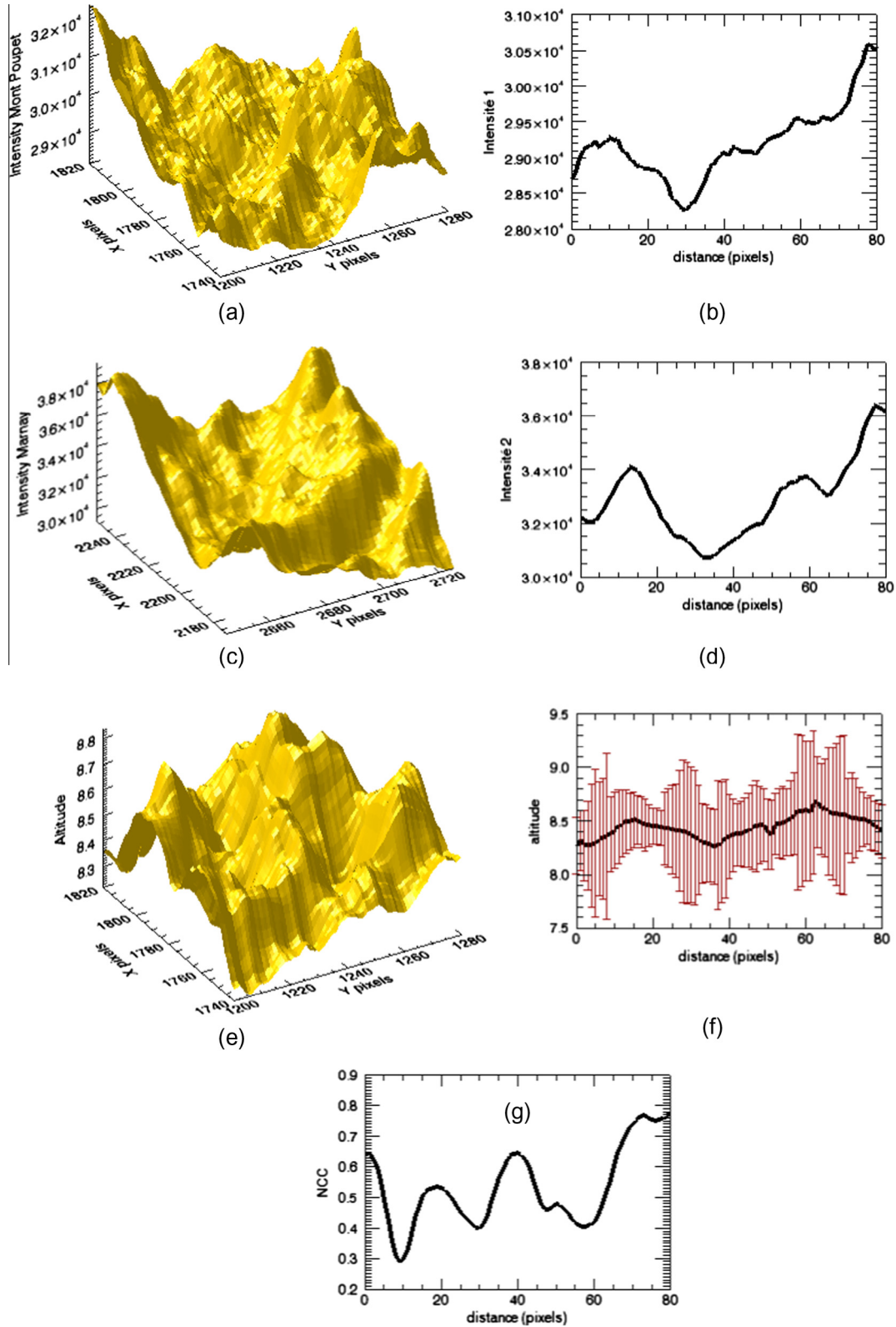Fig. 9. Change in the ZNCC versus the average altitude.

Fig. 10. 3D reconstruction of natural cirrus in 11 June 2014. (a) and (c) pseudo-relief representations of the intensity measured at Mont Poupet (a) and Marnay (c). Panels (b) and (d) present a cut of intensities. In panel (e) a 3D topographic map of the altitude of cirrus clouds barycenter. (f) a cut of the relief map profile of the barycenter altitude. The panel (g) gives the value of the coefficient of cross-correlation (ZNCC).
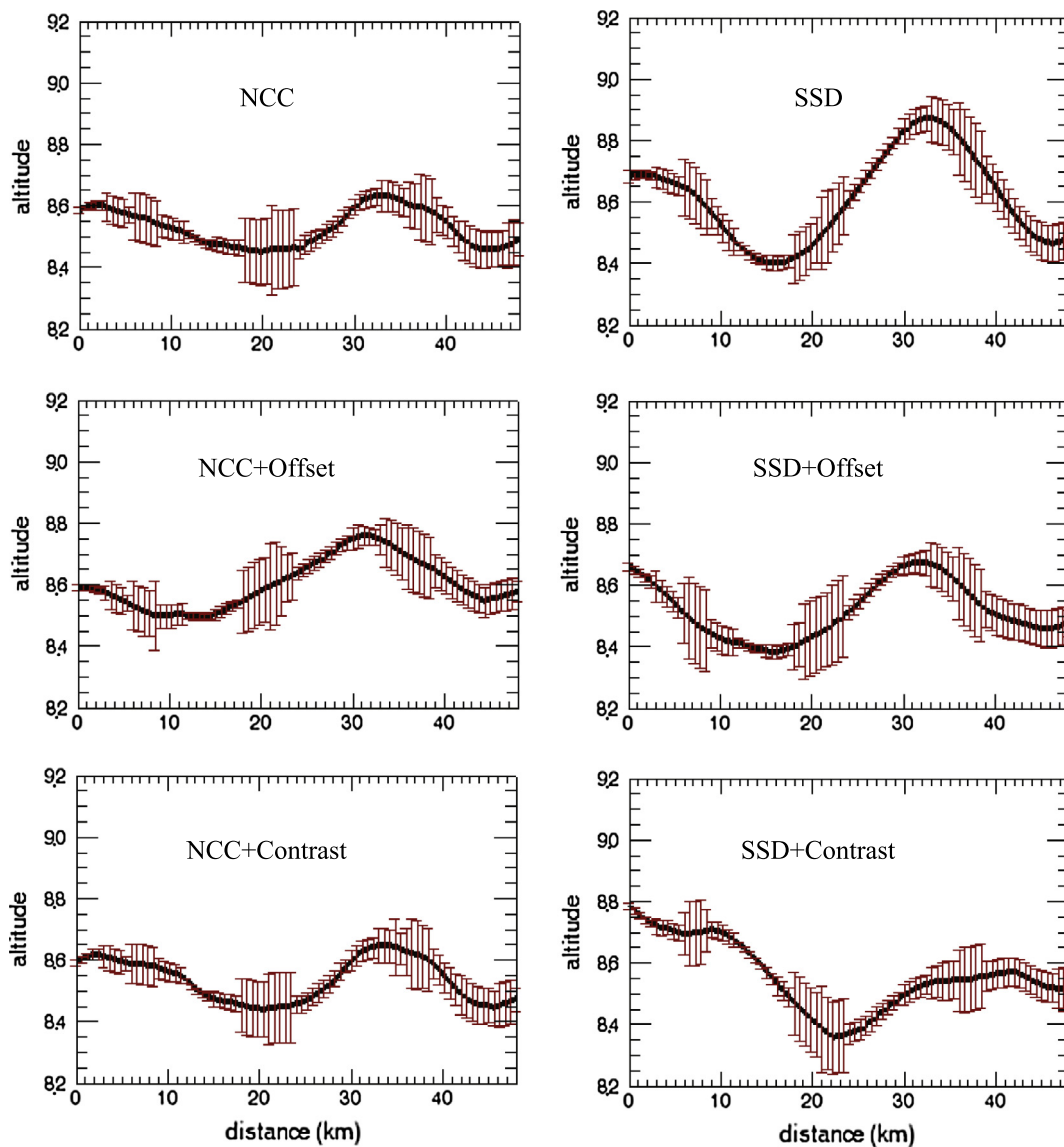
Fig. 11. Results of the comparison between the ZNCC and ZSSD coefficients.

Table 1
Comparison between a coefficient ZNCC and ZSSD.

	Average altitude (km)	Amplitude (km)	Alt_{min} (km)	Alt_{max} (km)
ZNCC	8.59	0.2	8.45	8.65
ZNCC + offset	8.62	0.23	8.49	8.72
ZNCC + contrast	8.59	0.2	8.45	8.65
ZSSD	8.66	0.47	8.4	8.87
ZSSD + offset	8.54	0.31	8.38	8.69
ZSSD + contrast	8.52	0.45	8.35	8.8

results are less sensitive to changes in contrast and to the presence of a continuous component. In all three tests, the results obtained with the NCC are: 8.59, 8.62 and 8.59 km for altitude and 0.2, 0.23 and 0.2 km for the amplitude.

6. Conclusion

In this paper, we discussed the problem of 3D reconstruction using photometric and geometric methods of a stereoscopic system for tropospheric cirrus clouds.

The important point of this work is to develop an original method for stereo-imaging based on the matching of two images of the same object acquired in two different sites. For the matching of the two images, we calculate for each pair of points, a parameter called ZNCC (Zero mean Normalized Cross-Correlation) or the coefficient of the zero mean sum of squares of differences called ZSSD. Our work allowed us to characterize and to perform measurements on structures diffuse with no well-defined contour.

Regarding the application, we used two cameras Canon 400D. The images were taken also in the mode vis-à-vis two sites located in Franche-Comté: Mont Poupet and Marnay.

We characterized the type "cirrus" clouds that are formed in the upper troposphere. Clouds play an important role in the mechanisms of climate. In addition, artificial cirrus clouds are created by the contrails of aircraft, and add a significant contribution to the processes of air pollution.

Cirrus clouds have a special place in climate research. Their presence was observed on the completeness of the globe, and the technical means of today offer finally the opportunity to be able to study them correctly. Moreover, the complexity of their radiative and optical properties is unique among the clouds.

The principles of stereoscopic and inversion projection applied seem conclusive, but can be improved. In particular, the matching methods used for the 3D restitution must be studied to determine how to apply them to diffuse objects such as structures of cirrus clouds.

In future work, other additional measurements will be considered such as ground atmospheric soundings conducted by the lidar on the CALIPSO satellite and lidars located at the LATMOS Laboratory at Saint-Michel l'Observatoire.

References

Aschwanden, P., Guggenbuhl, W., 1992. Experimental results from a comparative study on correlation-type registration algorithms. In: Forstner, W., Ruwiedel, S. (Eds.), Robust Computer Vision. Wichmann, pp. 268–289.

Beyer, H.A., 1992. Accurate calibration of CCD-cameras. In: Computer Vision and Pattern Recognition. Proceedings CVPR'92, IEEE Computer Society Conference, pp. 96–101.

Cadet, B., Giraud, V., Haeffelin, M., et al., 2005. Improved retrievals of the optical properties of cirrus clouds by a combination of lidar methods. Appl. Opt. 44, 1726–1734.

Cotton, W.R., Bryan, G.H., Van de Heever, S.C., 2011. Storm and Cloud Dynamics, vol. 99. Academic press.

Dowling, D.R., Radke, L.F., 1990. A summary of the physical properties of cirrus clouds. J. Appl. Meteorol. 29, 970–978.

Ehrlich, A., Bierwirth, E., Wendisch, M., Herber, A., Gayet, J.-F., 2012. Airborne hyperspectral observations of surface and cloud directional reflectivity using a commercial digital camera. Atmos. Chem. Phys. 12 (7), 3493–3510.

Fanany, M.I., Kumazawa, I., 2004. A neural network for recovering 3D shape from erroneous and few depth maps of shaded images. Pattern Recogn. Lett. 25, 377–389.

Fauchez, T., Cornet, C., Szczap, F., Dubuisson, P., Rosambert, T., 2014. Impact of cirrus clouds heterogeneities on top-of-atmosphere thermal infrared radiation. Atmos. Chem. Phys. 14 (11), 5599–5615.

Faugeras, O., 1994. A Geometrric ViewPoint. Three-dimensional computer vision. MIT Press.

Faugeras, O.D., Hotz, B., Mathieu, H., Vieville, T., Zhang, Z., Fua, P., Theron, E., Moll, L., Berry, G., Vuillemin, J., Bertin, P., Proy, C., 1993. Real Time Correlation-Based Stereo: Algorithm, Implementations and Applications, INRIA, Tech. Rep. RR-2013.

Fontana, F., Lugrin, D., Seiz, G., Meier, M., Foppa, N., 2013. Inter comparison of satellite-and ground-based cloud fraction over Switzerland (2000–2012). Atmos. Res. 128, 1–12.

Fua, P., Leclerc, Y.G., 1995. Object-centered surface reconstruction: combining multi-image stereo and shading. Int. J. Comput. Vision 16, 35–56.

Ghanem, R.N., Ramanathan, C., Jia, P., Rudy, Y., 2003. Heart-surface reconstruction and ECG electrodes localization using fluoroscopy, epipolar geometry and stereovision: application to noninvasive imaging of cardiac electrical activity. IEEE Trans. Med. Imaging 22, 1307–1318.

Hartley, R., Zisserman, A., 2003. Multiple View Geometry in Computer Vision. Cambridge University Press.

Hirsch, E., Agassi, E., Koren, I., 2011. A novel technique for extracting clouds base height using ground base imaging. Atmos. Meas. Tech. 4, 17–130.

Kataoka, R., Miyoshi, Y., Shigematsu, K., Hampton, D., Mori, Y., Kubo, T., Yamashita, A., Tanaka, M., Takahei, T., Nakai, T., Miyahara, H., Shiokawa, K., 2013. Stereoscopic determination of all-sky altitude map of aurora using two ground-based Nikon DSLR cameras. Ann. Geophys. 31 (9), 1543–1548.

Keckhut, P., Hauchecorne, A., Bekki, S., Colette, A., David, C., Jumelet, J., 2005. Indications of thin cirrus clouds in the stratosphere at midlatitudes. Atmos. Chem. Phys., 3407–3414

Kouahla, M.N., Moreels, G., Faivre, M., Clairemidi, J., Meriwether, J. W., Lehmacher, G.A., Veliz, O., 2010. 3D imaging of the OH mesospheric emissive layer. Adv. Space Res. 45 (2), 260–267.

Liu, L., Sun, X.J., Liu, X.C., Gao, T.C., Zhao, S.J., 2015. Comparison of cloud base height derived from a ground-based infrared cloud measurement and two ceilometer. Adv. Meteorol. 2015.

Ma, Y., 2004. An Invitation to 3-D Vision: From Images to Geometric Models. Springer Science & Business Media.

Mallet, A., Lacroix, S., Gallo, L., 2000. Position estimation in outdoor environments using pixel tracking and stereovision. In: Robotics and Automation. Proceedings ICRA'00. IEEE International Conference, pp. 3519–3524.

Manoj, S.O., Kavitha, V., Arul, J.S., 2010. Recognizing the cloud type and estimation of rainfall. In: Proceedings of the International Conference on Communication and Computational Intelligence, India, pp. 178–183.

Menzel, W.P., 2001. Cloud tracking with satellite imagery: from the pioneering work of Ted Fujita to the present. Bull. Am. Meteorol. Soc. 82, 33–47.

Moreels, G., Clairemidi, J., Faivre, M., Mougin-Sisini, D., Kouahla, M. N., Meriwether, J.W., Veliz, O., 2008. Stereoscopic imaging of the hydroxyl emissive layer at low latitudes. Planet. Space Sci. 56, 1467–1479.

Park, S.K., Kweon, I.S., 2001. Robust and direct estimation of 3-D motion and scene depth from stereo image sequences. Pattern Recogn. 32, 1713–1728.

Pautet, D., Moreels, G., 2002. Ground-based satellite-type images of the upper atmosphere emissive layer. Appl. Opt. 41, 823–831.

Perrollaz, M., Labayrade, R., Royere, C., et al., 2006. Long range obstacle detection using laser scanner and stereovision. In: Intelligent Vehicles Symposium. IEEE, pp. 182–187.

Ramanathan, V., Collins, W., 1991. Thermodynamic regulation of ocean warming by cirrus clouds deduced from observations of the 1987 El Nino. Nature 351, 27–32.

Sassen, K., 1997. Contrail-cirrus and their potential for regional climate change. Bull. Am. Meteor. Soc. 78, 1885–1903.

Schafer, K., Emeis, S.M., Rauch, A., Munkel, C., Vogt, S., 2004. Determination of mixing layer heights from ceilometer data. Remote Sens. Int. Soc. Optics Photonics, 248–259.

Stubenrauch, C.J., Rossow, W.B., Kinne, S., Ackerman, S., Cesana, G., Chepfer, H., Di Girolamo, L., Getzewich, B., Guignard, A., Heidinger, A., Maddux, B.C., Menzel, W.P., Minnis, P., Pearl, C., Platnick, S., Poulsen, C., Riedi, J., Sun-Mack, S., Walther, A., Winker, D., Zeng, S., Zhao, G., 2013. Assessment of global cloud datasets from satellites: project and database initiated by the GEWEX radiation panel. Bull. Am. Meteorol. Soc. 94 (7), 1031–1049.

Sunilkumar, S.V., Parameswaran, K., 2005. Temperature dependence of tropical cirrus properties and radiative effects. J. Geophys. Res. Atmos. 110 (D13).

Tapakis, R., Charalambides, A.G., 2013. Equipment and methodologies for cloud detection and classification: a review. Sol. Energy 95, 392–430.

Tsai, R.Y., 1987. A versatile camera calibration technique for high-accuracy 3D machine vision metrology using off-the-shelf TV cameras and lenses. IEEE J. Rob. Autom. 3, 323–344.

Wylie, D.P., Menzel, W.P., 1999. Eight years of high cloud statistics using HIRS. J. Clim. 12, 170–184.